Journal of Systems Engineering and Electronics
Vol. PP, No. 99, April 2023, pp.1 – 7

Three-channel CMOS transimpedance amplifier for LiDAR sensor receiver

LIU Ruqing, ZHU Jingguo*, JIANG Yan, LI Feng, JAING Chenghao, and MENG Zhe

Photoelectric R & D Center, Academy of Opto-Electronics, Chinese Academy of Sciences, Beijing 100094, China

Abstract: For time-of-flight (TOF) light detection and ranging (LiDAR), a three-channel high-performance transimpedance amplifier (TIA) with high immunity to input load capacitance is presented. A regulated cascade (RGC) as the input stage is at the core of the complementary metal oxide semiconductor (CMOS) circuit chip, giving it more immunity to input photodiode detectors. A simple smart output interface acting as a feedback structure, which is rarely found in other designs, reduces the chip size and power consumption simultaneously. The circuit is designed using a 0.5 μm CMOS process technology to achieve low cost. The device delivers a 33.87 dBΩ transimpedance gain at 350 MHz. With a higher input load capacitance, it shows a −3 dB bandwidth of 461 MHz, indicating a better detector tolerance at the front end of the system. Under a 3.3 V supply voltage, the device consumes 5.2 mW, and the total chip area with three channels is 402.8×597.0 μm^2 (including the test pads).

Keywords: transimpedance amplifier (TIA), three-channel, regulated cascade (RGC), light detection and ranging (LiDAR).

DOI: 10.23919/JSEE.2023.000058

1. Introduction

Target detection, advanced driver assistance systems (ADAS), and autonomous piloted driving are application examples of light detection and ranging (LiDAR) technologies that have sparked a lot of interest recently. However, these applications require low-cost, low-power, and compact three-dimensional LiDARs [1−3]. For detecting and processing the reflected signals from targets, LiDAR uses laser light to characterize targets across a scene [4,5]. Laser, atmospheric optics, target and environment features, radars, mechatronics, and computer technologies are used simultaneously in LiDARs [6,7]. The so-called time-of-flight (TOF) sensors, which measure the transit time (ΔT) of a laser pulse to the target and back to the receiver, are used in advanced rapidly-growing LiDAR sensors with imaging capacity. The pulsed TOF methods, however, rely on the use of short, generally ns-scale laser pulses, necessitating the employment of precise wide-band signal processing techniques [8−10].

The design of a generic type of TOF consists of a pulsed laser transmitter, photodetector and receiver optics, and a preamplifier and comparator (CMP) receiving device [11]. Then, the ranging result is obtained through the time-to-digital converter (TDC) and field programmable gate array (FPGA) data processing. The reflected LiDAR signal of the target is usually a Gaussian pulse. Its level varies widely as a function of the distance. For the best accuracy, the LiDAR receiver requires wide bandwidth and appropriate gain amplifier. Also, the gain should be as controlled as possible to minimize degradation of the signal to noise radio (SNR) before any distortion occurs [12].

LiDAR systems often use arrays of light-emitting diodes (LEDs), avalanche photodiode detectors (APDs), or laser diodes (LDs) to diffusely illuminate targets in the scene. Due to their basic electro-optical architecture and low-cost implementations, these sensors appear to have sparked a lot of attention [13]. However, the parasitic capacitance of some types of APDs in these sensors is in the range of 1 pF to 10 pF [14], although most researchers use a 2 pF standard as the usual detector capacitance [15,16]. As a result, for the LiDAR receiving system, a preamplifier insensitive to the parasitic capacitance of the detectors must be considered during design.

As shown in Fig. 1, the preamplifier is the key module in the front-end receiver of the LiDAR system. It transforms and amplifies the photodetector's weak current signal into a voltage signal. Because the preamplifier has such a strong influence on system requirements such as sensitivity, speed, and stability, selecting the circuit settings for the best performance necessitates extensive design work. As a front-end circuit, a voltage-mode inverter (INV) TIA has been conventionally utilized

Manuscript received November 08, 2021.
*Corresponding author.

[17−19]. However, due to the intrinsic design trade-off between gain and bandwidth (BW), the INV-transimpedance amplifier (TIA) gain is limited, which may result in a significant noise rise and sensitivity loss [20]. This would lead to a shorter detection range unless laser power is increased. In general, TIA is utilized in preamplifiers. However, in this paper, we propose a novel diode metal oxide semiconductor (MOS) feed-forward TIA. As a result, the three-channel TIA parallel array in 0.5 μm CMOS technology provides a low-cost and low-area solution for the front-end receiver in LiDAR applications, thanks to its strong immunity to the parasitic capacitance of the detectors.

The rest of the paper is organized as follows. Section 2 describes the TIA's construction and operation, as well as its characteristics. Section 3 shows the layout design and simulation results. Section 4 summarizes the test results obtained with the entire chip. Section 5 concludes the paper with a summary of the findings.

2. System design

The three-channel TIA which comprises a micro-optic module, a three-channel parallel optical receiver preamplifier amplifier and a dummy amplifier is shown in Fig. 1. Three-channel parallel input optical signals are connected to a three-channel photo-detector, which converts these optical signals to electric current signals and transmits them to three-channel preamplifiers to produce output signals.

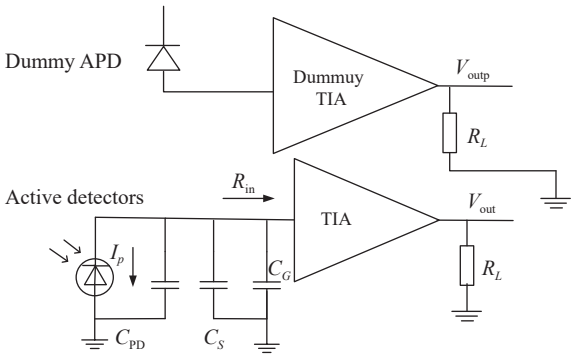

Fig. 1 Proposed three-channel transimpedance preamplifier

Fig. 1 and Fig. 2 depict the schematic of the proposed transimpedance preamplifier. R_L is the load resistance, V_{outp} is the dummy output voltage, and V_{out} is the real output voltage. The photodetector is represented by current source I_P. C_{PD} may be treated as the parasitic capacitance of the photodiode, which is in the range of 1 pF to 10 pF. C_s and C_G denote the parasitic capacitance of transimpedance preamplifier. $C_{PD}+C_s+C_G=C_T$. R_{in} is the equivalent input resistance.

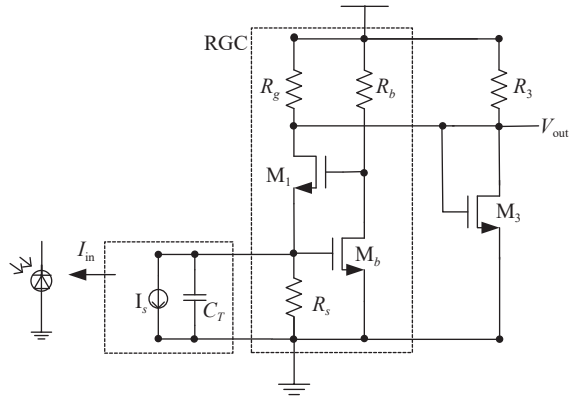

Fig. 2 Schematic of the proposed diode MOS feedforward TIA

CMOS M_1 and M_b, resistance R_g, R_s, and R_b constitute an RGC input stage. A diode MOS M_3 is selected to operate as the feedforward to the regulated cascade (RGC) to maximize the transconductance and increase the gain BW.

The design criteria for TIAs in LiDAR systems include variable transimpedance gain, low input impedance, and wide BW for narrow-pulse recovery, low noise current spectral density for weak reflected signal detection, and low power dissipation per channel for chip reliability.

2.1 Input impedance

As the common-gate input stage, transistors M_1 and M_b and the resistance R_g is the RGC stage, the bias voltage of M_1 is provided by the common-source stage: transistor M_b and resistance R_b. The RGC input stage is stable enough thanks to the feedback loop. Fig. 3 shows the small-signal equivalent circuit of RGC structure, and the equivalent input resistance R_{in} is shown as follows:

$$I_{in} = -g_{m_1} V_1 = -g_{m_1}(V_b - V_{in}), \tag{1}$$

$$V_b = -g_{m_b} V_{in} R_b, \tag{2}$$

$$R_{in} = \frac{v_{in}}{I_{in}} = \frac{1}{g_{m_1}(1 + g_{m_b} R_b)}, \tag{3}$$

where I_{in} is the equivalent input current, g_{m_1} is the transconductance of M_1. V_1 is the voltage of M_1. V_b is the voltage of the resistance R_b. V_{in} is the input voltage. g_{m_b} is the transconductance of M_b.

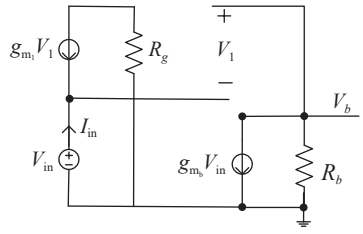

Fig. 3 Small signal equivalent circuit of RGC

The circuit shows current stability as a result of the feedback. When the M_1 drain source current increases, the voltage difference R_s increases, the CMOS M_b gate voltage increases, and the M_b source current increases. As a result, the voltage difference R_s grows larger, and the M_b gate voltage decreases. Therefore, the source current of M_1 decreases and it stabilizes the DC operating point of the circuit.

2.2 Transimpedance gain

The basic structure of the preamplifier is the voltage parallel negative feedback with R_f, as shown in Fig. 4(a), in the direct current (DC) case, its closed-loop gain is $-R_f$. However, in most CMOS technologies, perfectly controlled resistance levels or precise and suitable physical dimensions are difficult to achieve. Therefore, instead of a feedback resistance, a diode-connected MOS structure of M_3 is used in this paper, as shown in Fig. 4(b). Its impedance is roughly $1/g_{m3}$, where g_{m3} is the transconductance M_3. The M_3 not only ensures chip processing accuracy but also reduces the layout area. This type of feedback is uncommon in other designs. When the process parameters are fixed, the aspect ratio of M_3 can be decreased to increase the circuit's gain.

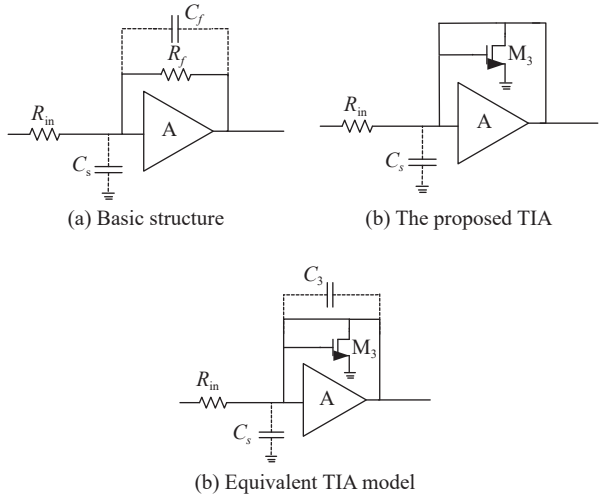

Fig. 4 Basic structure of the proposed diode MOS feedforward TIA

2.3 BW

Usually, the bandwidth of the RGC circuit is given as

$$\mathrm{BW} = 1/2\pi R_g C_{\mathrm{d1}}$$

where C_{d1} is the drain capacitance of M_1. Based on the resistance and capacitance parameters of the detector, the equivalent load diagram of the preamplifier circuit designed in this work is shown in Fig. 1 and Fig. 4. In Fig. 4(a), C_s and R_f introduce a zero-point in the amplitude-frequency plot of the closed-loop system which affects the stability of the circuit. To compensate the zero point, the normal technique is to add a compensated capacitance, as shown in Fig. 4(a). A compensation capacitor C_f is connected in parallel to R_f to form a phase complement between the $R_{\mathrm{in}}C_f$ and R_fC_s networks. Thus, a pole P_0 is generated into the amplitude-frequency plot. The frequency of the pole is f=1/2πR_fC_f. Therefore, the pole counteracts the influence of the zero point, thus keeping the whole loop stable. The parasitic capacitance C_3 of M_3 can also be employed as a compensation capacitor, thanks to the bulk effect of the diode connection M_3 presented in this study. Consequently, the BW of the circuit is

$$f = g_{\mathrm{m3}}/2\pi C_3$$

where C_3 is proportional to the length and width of M_3 pipeline channel. Here, M_3 and R_3 should be carefully chosen in the circuit, hence giving rise to the well-known design tradeoff between gain (which is directly proportional to M_3 channel length) and BW (which is inversely proportional to the input resistance and thus to M_3).

2.4 Noise

Using Kirchhoff's current law, the input-referred equivalent noise power spectral density of the TIA shown in Fig. 5 can be calculated using

$$\begin{aligned} i^2_{n,eq} = {} & \frac{4kT}{R_s} + \frac{4kT}{R_g} + \frac{4kT}{R_3} + 2qI_1 + 2qI_3 + 2qI_{gb} + \\ & 4kT\gamma g_{\mathrm{m_1}}\left[\frac{(1+\omega C_t R_s)^2}{(1+g_{\mathrm{m_1}}R_s)^2 + (\omega C_t R_s)^2}\right] + \\ & \frac{4kT\gamma}{g_{\mathrm{m_b}}}[\frac{1}{R_s} + (\omega C_t)^2] + \\ & \frac{4kT\gamma}{g_{\mathrm{m_3}}}\left[\left(\frac{1}{R_s}+\frac{1}{R_1}\right)^2 + \omega^2(C_{\mathrm{gs3}} + C_{\mathrm{gd1}} + C_{\mathrm{gd3}})^2\right] \end{aligned} \tag{4}$$

where $C_t = C_{\mathrm{gdb}} + C_{\mathrm{gs1}}$, γ=2/3, k is Boltzmann constant, T is the absolute temperature. C_{gsb}, C_{gdb}, C_{gs1}, C_{gd1}, C_{gs3}, and C_{gd3} represent the gate-source capacitances and the gate-drain capacitances of M_{b}, $M_{1,}$ and M_3. q is the electionic charge quantity, I_1 is the average DC of M_1, I_3 is the average DC of M_3, I_{gb} is the average DC of M_b, and w=$g_{\mathrm{m1}}/c_{\mathrm{gs1}}$. Equation (4) indicates that the thermal noise of R_1, R_3, and R_g is dominant at low frequencies whereas g_{m_1}, g_{m_b}, and g_{m_3} become the critical factors to determine the high-frequency noise. There are two main approaches for improving noise performance as follows: increasing

R_1, R_3, and R_g lowers the low-frequency noise. Increasing M_b's gate width improves gmb's value, hence M_b's gate width has an optimum value for achieving the smallest equivalent input noise current power spectrum density. The values of g_m, on the other hand, should be carefully chosen to maximize the design tradeoff between input resistance, bandwidth, and high-frequency noise.

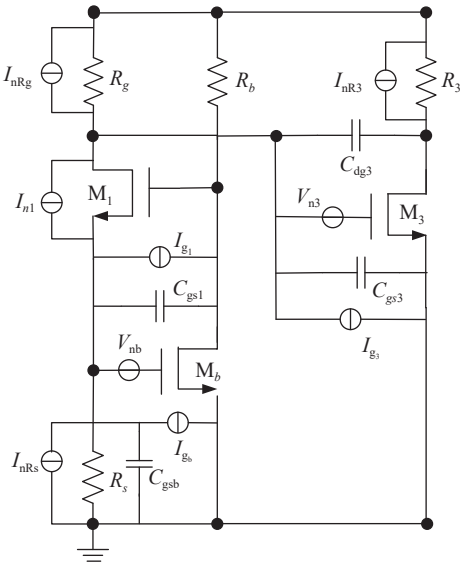

Fig. 5 Equivalent noise model of the TIA

3. Layout design and simulation results

Post-layout simulations are performed for the proposed diode MOS feedforward TIA by using the model parameters of a 0.5 μm CMOS technology. The post layout is shown in Fig. 6. The number of pads is kept at 11, which accounts for more than a third of the entire design space for ease of testing.

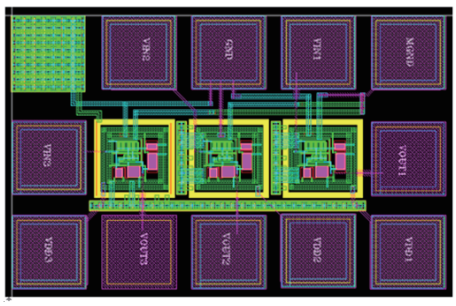

Fig. 6 Three-channel parallel array layout

The total area of the layout is 402.8×597.0 μm^2. The total power consumption is 5.2 mW under 3.3 V voltage operation. The photodiode is electrically modeled as a current source with a parasitic capacitance of 5 pF and 10 pF, and parasitic resistance of 50 Ω in simulations to demonstrate that the diode MOS feedforward TIA has good immunity to its input photodiode capacitance. The parasitic capacitance from the input/output (I/O) pads and the electro-static disharge (ESD) protection diodes are included in the simulations. Table 1 and Fig. 7 present the simulation results.

Table 1 Three channel post-layout simulation results (100 MHz)

Channel	Input C_s/pF	Bandwidth/ MHz	Output voltage/V	Noise/ (pA·s^{-1})	Gain/ dBΩ
1	5	739.9	0.4−2	3.051	41.01
2	5	750.7	0.4−2	3.058	40.09
3	5	827.7	0.4−2	3.049	41.03
1	10	612.8	0.5−2	3.749	40.09

For Table 1, typical nMOS and typical pMOS in corner analysis are conducted at 27°C. There are three channels in this design, and the performance of each channel is tested respectively. It can be seen from the first three rows that the performance of the three channels is basically the same. When the capacitance of 5 pF is added at the input end, the chip BW is greater than 700 MHz and the input noise performance is stable. From the comparison of the first line with the last line, it can be seen that even if the load capacitance is increased by up to 10 pF at the input, the chip bandwidth is greater than 600 MHz, and the noise performance is basically stable.

From Fig. 7 and Table 1, it is clearly seen that the diode MOS feedforward TIA achieves transimpedance gain and lower noise current spectral density, which can meet the essential design requirements of LiDAR. In other words, the product of transimpedance gain and BW is greatly improved while the noise penalty is minimal. It is also worth noting that the input dynamic range is 60 dB, and the power supply rejection ratio (PSRR) is 50 dB.

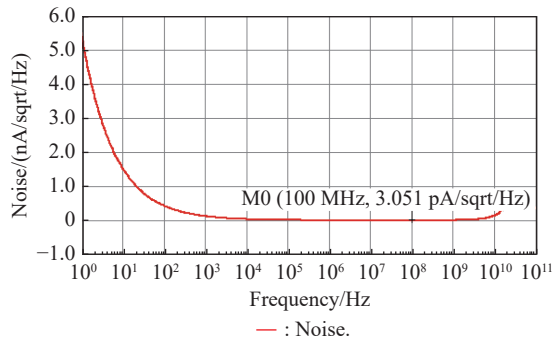

Fig. 7 Post-layout simulated input noise current spectral density of the TIA

4. Measurement data

This diode MOS feedforward TIA is fabricated in the 0.5 μm standard CMOS technology. Fig. 8(a) shows a

chip photomicrograph of the preamplifier. The printed circuit board (PCB) is shown in Fig. 8(b).

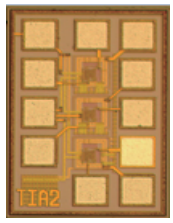

(a) Preamplifier chip photomicrograph

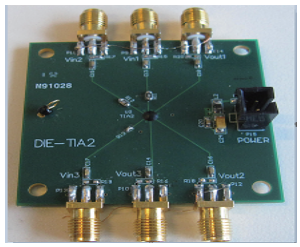

(b) PCB test board

Fig. 8 Images of the chips

After finishing the design, the performance of the front-end preamplifier is tested and verified in an Agilent open laboratory setup using the test PCB. Fig. 9 shows the schematic diagram of the test setup. The transimpedance gain and bandwidth are measured by generating a single-ended current signal from a 50 Ω output of Agilent vector network analyzer (E5071C) with a resistive attenuator. Fig. 10 shows the measured S-parameters (S_{21} and S_{11}) responses.

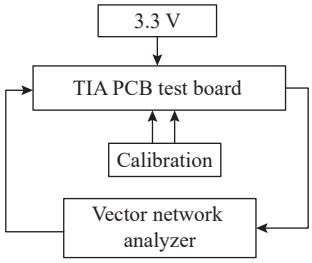

Fig. 9 Schematic diagram of the gain and bandwidth measurement

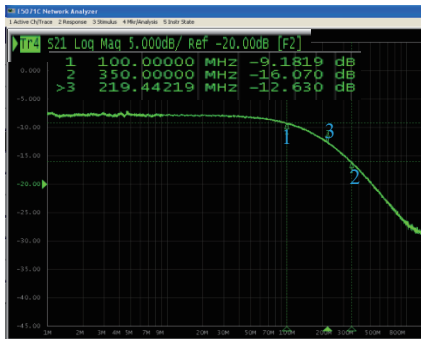

(a) S_{21} parameter

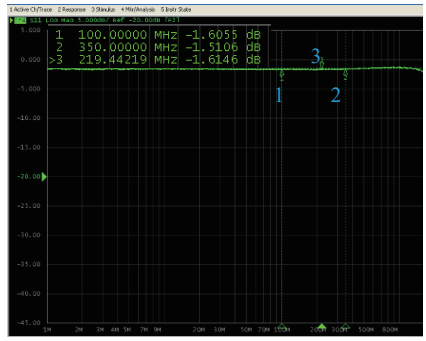

(b) S_{11} parameter

Fig. 10 Measured S-parameters

The transimpedance gain plot can be obtained as shown in Fig.11 with 5 pF parasitic capacitance load [21] as follows: $|Z_{TIA}| = |Z_0| \times |S_{21}| / |1 - S_{11}|$. The transimpedance gain is evaluated to be 33.87 dBΩ and the −3 dB BW is 461 MHz. Z_0 is 50 Ω.

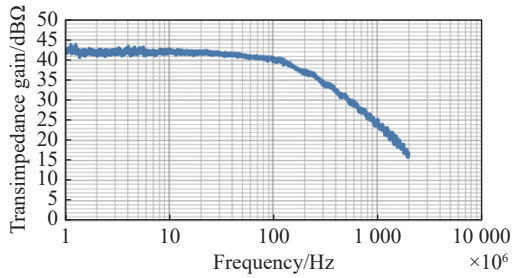

Fig. 11 Gain response of the TIA

Fig. 12 shows the measured noise spectrum from the Agilent spectrum analyzer (N9020MAX), which has the basic noise of −166 dBm. It can also be used to calculate the equivalent input noise current spectral density. The equivalent input noise current spectral density of the preamplifier is found to be 26.17 Pa/ $\sqrt{\text{Hz}}$.

Fig. 12 Gain response of the TIA

Table 2 compares the performance of the proposed TIA with other reported TIAs. The circuit in [12] shows better transimpedance gain performance than this work with the 5 pF input capacitance load. However, its −3 dB

BW is worse with large power consumptions. Compared to [17,18], the proposed TIA circuit has wider BW and lower power consumptions, indicating a better detector tolerance at the front end of the system.

Table 2 Perform comparison of published TIA circuits

Channel	The proposed circuit	[12]	[22]	[23]
Input C_s/pF	5	5	1.5	2
f_{-3dB}/MHz	461	170	150	50
Gain/dBΩ	33.92	113	106	106
Power/mW	5.2	250	165	12.6
Chip size/mm^2	0.4×0.6	3×3	0.9	–

5. Conclusions

A three-channel high-performance TIA has been designed and produced for use in the TOF LiDAR sensor receiver. Chip gain, 3 dB BW, noise, and other performance parameters are improved by using the RGC input structure and a diode-connected MOS output stage. In addition, CSMC 0.5 m CMOS technology is used to keep the chip's cost low. The TIA has high immunity to the parasitic capacitances of the detectors in the LiDAR receiving system, as demonstrated by the measured results. The entire chip integration of the array of receiving circuits for use in LiDAR is performed.

References

[1] YE L C, ZHANG G F, YOU Z, et al. A 2D resonant MEME scanner with an ultracompact wedge-like multiplied angle amplification for miniature LIDAR application. Proc. of the IEEE Conference on Sensors, 2016. DOI: 10.1109/ICSENS.2016.7808932.

[2] YU Y, LIU B, CHEN Z, et al. Photon counting LIDAR based on true random coding. Sensors, 2020, 20(11): 3331–3338.

[3] RAFAELA B S, SOUZA-FILHO P W M, SIMARD M, et al. Improving mangrove above-ground biomass estimates using LiDAR. Estuarine, Coastal and Shelf Science, 2020, 236: 106585.

[4] KIM S G, JUNG S H, YING X, et al. A 1. 8Gb/s/ch 10mw/ch −23dB crosstalk eight-channel transimpedance amplifier array for LADAR systems. Proc. of the International SOC Design Conference, 2013: 115–118.

[5] NGO T H, KIM C H, KWON Y J, et al. Wideband receiver for a three-dimensional ranging LADAR system. IEEE Trans. on Circuits and Systems, 2013, 60(2): 448–456.

[6] SUDHAKAR P, SHEELA K A, SATYANARAYANA M. Imaging lidar system for night vision and surveillance applications. Proc. of the 4th International Conference on Advanced Computing and Communication Systems, 2017. DOI: 10.1109/ICACCS.2017.8014690.

[7] KURTTI S, NISSINEN J, KOSTAMOVAARA J. A wide dynamic range CMOS laser radar receiver with a time-domain walk error compensation scheme. IEEE Trans. on Circuits and Systems, 2017, 64(3): 550–561.

[8] CHEN J D, HO H L, TSAY H L, et al. 3D chaos lidar system with a pulsed master oscillator power amplifier scheme. Optics Express, 2021, 29(17): 27871–27881.

[9] STROTKSMP M, ELSEN F, LHRING J, et al. Two stage innoslab amplifier for energy scaling from 100 to >500mJ for future LIDAR applications. Applied Optics, 2017, 56(10): 2886–2892.

[10] ZHU Y D, YANG J X, ZHANG X X, et al. Performance improvement of spaceborne carbon dioxide detection IPDA LIDAR using linearty optimized amplifier of photo-detector. Remote Sensing, 2021, 13(10): 2007.

[11] HONG C, KIM S H, KIM J H, et al. A linear-mode LiDAR sensor using a multi-channel CMOS transimpedance amplifier array. IEEE Trans. on Sensors, 2018, 18(17): 7032–7040.

[12] RUOTSALAINEN T, PALOJARVI P, KOSTAMOVAARA J. A wide dynamic range receiver channel for a pulsed time-of-flight laser radar. Journal of Solid-State Circuits, 2001, 36(8): 1228–1238.

[13] NICLASS C, SOGA M, MATSUBARA H, et al. A 0.18μm CMOS SOC for a 100-m-range 10-frame/s 200×96-pixel time-of-flight depth sensor. IEEE Journal of Solid-State Circuits, 2014, 49(1): 315–330.

[14] ZAND B, PHANG K, JOHNS D A. A transimpedance amplifer with DC-coupled differential photodiode current sensing for wireless optical communications. Proc. of the IEEE Custom Intergrated Circuits Conferencs, 2001: 455–458.

[15] CHO H S, KIM C H, LEE S G. A high-sensitivity and low-walk error LADAR receiver for military application. IEEE Trans. on Circuits and Systems, 2014, 61(10): 3007–3015.

[16] ZHOU Y X, ZHAO Y, YANG J. A broadband AGC transimpedance amplifier for automotive LiDAR. Microelectronics, 2019, 49(6): 755–759.

[17] ZHENG H, MA R, LIU M L, et al. A linear dynamic range receiver with timing discrimination for pulsed TOF imaging LADAR application. IEEE Trans. on Instrumentation and Measurement, 2018, 67(11): 2684–2691.

[18] CHENG L, RUI B, SHAFIK A, et al. Silicon photonic transceiver circuits with microring resonator bias-based wavelength stabilization in 65 nm CMOS. IEEE Journal of Solid-State Circuits, 2014, 49(6): 1419–1436.

[19] TSAI C M. A 40mW 3Gb/s self-compensated differential transimpedance amplifier with enlarged input capacitance tolerance in 0. 18μm CMOS technology. IEEE Journal of Solid-State Circuits, 2009, 44(10): 2671–2677.

[20] YANG Y X, GAO J B, SONG H Z. et. al. Near-infrared array receiver for real-time 3D imaging application. Proc. of the 4th Optoelectronics Global Conference, 2019: 89–93.

[21] LIU R Q, JIANG Y, JIANG C H, et al. Amplifying circuit interface model for lidar signal processing system. Journal of Electronics & Information Technology, 2020, 42(7): 1636–1642.

[22] HAO Z, RUI M, LIU M, et al. A linear dynamic range receiver with timing discrimination for pulsed TOF imaging LADAR application. IEEE Trans. on Instrumentation and Measurement, 2018, 67(11): 2684–2691.

[23] MA R, LIU M, ZHENG H, et al. A 77 dB dynamic range low power variable-gain transimpedance amplifier for linear LADAR. IEEE Journal of Circuits and Systems, 2018, 65(2): 171–175.

Biographies

LIU Ruqing was born in 1987. She received her M.S. degree in microeletronics and solid state electronics from Beijing Institute of Technology. She is an engineer in Microelectronics Research Institute, Chinese Academy of Sciences. Her research interest is LiDAR field progrmmable gate array signal processing.
E-mail: liuruqing@ime.ac.cn

ZHU Jingguo was born in 1977. He received his Ph.D. degree in computer application technology from the Chinese Academy of Sciences, where he is the leader of the lidar team. His research interests are lidar, intelligent sensing, and photoelectric countermeasure.
E-mail: zhujingguo@ime.ac.cn

JIANG Yan was born in 1985. He received his M.S. degree in microeletronics and solid state electronics from Beijing Institute of Technology. He is an engineer of Microelectronics Research Institute, Chinese Academy of Sciences. His research interest is lidar signal processing.
E-mail: jiangyan@ime.ac.cn

LI Feng was born in 1976. He received his Ph.D. degree in microeletronics and solid state electronics from Beihang University. He is an associate researcher in the Institute of Microelectronics, Chinese Academy of Sciences. His research interests are signal detection, embedded system, and electromechanical control.
E-mail: lifeng1@ime.ac.cn

JIANG Chenghao was born in 1987. He received his Ph.D. degree in instrument science and technology from Changchun University of Science and Technology. He is a researcher in the Institute of Microelectronics of Chinese Academy of Sciences. His research interests are laser detection technology and visual detection.
E-mail: Jiangchenghao@ime.ac.cn

MENG Zhe was born in 1979. He received his M.S. degree in software engineering from Chinese Academy of Sciences. He is an engineer in Institute of Microelectronics of the Chinese Academy of Sciences. His research interests are software engineering.
E-mail: mengzhe@ime.ac.cn